Journal of Infrastructure Intelligence and Resilience 4 (2025) 100181

Contents lists available at ScienceDirect

Journal of Infrastructure Intelligence and Resilience

journal homepage: www.journals.elsevier.com/journal-of-infrastructure-intelligence-and-resilience

Methodologies for functional recovery assessment of hilly roads situated in the Indian Himalayan region

Rahul Kumar [a], Mahipal Kulariya [b], Sandip Kumar Saha [a,*]

[a] School of Civil and Environmental Engineering, Indian Institute of Technology Mandi (IIT Mandi), Kamand, Himachal Pradesh, 175075, India
[b] Department of Civil Engineering, Indian Institute of Technology Bombay (IIT Bombay), Powai, Mumbai, 400076, India

ARTICLE INFO

Keywords:
Buildings
Earthquakes
Functional recovery time
Landslides
Resilience
Road network

ABSTRACT

Road networks are a critical component of the built environment and play a vital role in enhancing overall community resilience. Ensuring the safety and functionality of these networks is essential, especially in hilly regions such as the Indian Himalayan Region (IHR), which is highly vulnerable to multiple hazards such as earthquakes and earthquake-induced landslides. Past events in this region have demonstrated that the disruptions in road connectivity during such events lead to significant socio-economic losses by restricting access to essential services, impeding trade, and affecting tourism-based livelihoods. Therefore, this study proposes methodologies to identify critical road segments and systematically estimate the expected functional recovery of hilly roads in the IHR. The approach integrates a rapid visual screening-based technique to preliminarily assess potentially vulnerable buildings, hill cuts, and slopes that may obstruct roads. In addition, it provides a framework for incorporating detailed probabilistic methods to enable a more refined estimation of road functionality recovery. The applicability of the proposed methodologies is illustrated through a detailed case study. The insights gained from this work can support the development of effective mitigation strategies and guide resource allocation to restore the functionality of roads affected by earthquakes and earthquake-induced landslides.

1. Introduction

Road infrastructure is recognized as an essential part of the built environment and significantly contributes to strengthening community resilience. Roads are directly linked to nearly every function of a society, and disruption to their operation can significantly hinder the delivery of essential services. For effective post-hazard response, such as resettlement in affected areas, it is crucial to ensure that roads recover quickly and regain functionality to an acceptable level. As a result, the susceptibility of road networks to disruptions has emerged as a key focus in resilience studies (Matisziw and Murray, 2009; Furno et al., 2021). Road network disruptions are generally categorized into two types, namely, disruptions caused by natural events such as earthquakes, floods, landslides, and wildfires, and those resulting from human actions, including traffic accidents and infrastructure breakdowns (Huang and Loo, 2023). Depending on the intensity and location of the disruption, one or more components of the road network, such as intersections or road segments, may become non-operational. Enhancing the resilience of a roadway network requires identifying critical routes or paths that should be prioritized for improvement.

In recent years, several studies have focused on assessing and improving the resilience of road networks using graph theories (Freckleton et al., 2012; Das, 2020; Martín et al., 2021; Nipa and Kermanshachi, 2022; Serdar et al., 2022; Xu et al., 2021; Chen et al., 2023; Kazmi et al., 2023; Wang et al., 2023; Zhang et al., 2023; Alizadeh and Dodge, 2025; Mashrur and Kameshwar, 2025). Recent studies have also proposed efficient methods to identify critical road segments based on edge-based graph neural networks that rank the importance of road links for prioritizing recovery (e.g., Jana et al., 2023; Lu et al., 2024; Liu and Liu, 2025). However, due to the unique topography and demographic characteristics of hilly regions such as the Indian Himalayan Region (IHR), a seismically active and landslide-prone area (BIS, 2016; Kumar et al., 2017; Froude and Petley, 2018), these theories cannot be directly applied. Traditional methods based on graph theory typically employ connectivity-based measures (e.g., degree centrality, eigenvector centrality, commuter flow centrality), distance-based measures (e.g., closeness centrality, betweenness centrality), and time-based measures (e.g., time delay centrality, delay-flow centrality) to assess the resilience

* Corresponding author.
E-mail addresses: s22011@students.iitmandi.ac.in (R. Kumar), mahipalkulariya@iitb.ac.in (M. Kulariya), sandip_saha@iitmandi.ac.in (S.K. Saha).

https://doi.org/10.1016/j.iintel.2025.100181
Received 30 August 2025; Received in revised form 7 October 2025; Accepted 17 October 2025
Available online 20 October 2025
2772-9915/© 2025 The Authors. Published by Elsevier Ltd on behalf of Zhejiang University and Zhejiang University Press Co., Ltd. This is an open access article under the CC BY-NC-ND license (http://creativecommons.org/licenses/by-nc-nd/4.0/).

of a network system (Fang et al., 2016; Misra et al., 2017; Wan et al., 2021; Esfahani et al., 2024; Shafiei et al., 2025). However, in hilly regions, a key limitation is that alternative routes are often non-existent or severely limited, making these conventional approaches less effective. Consequently, restoring the functionality of major roads becomes critical for enabling emergency services to carry out rescue and recovery operations effectively. For instance, debris-flow risk assessment frameworks applied to highways in seismically active mountain areas (Peng et al., 2013; Zou et al., 2018; Jin et al., 2023) have highlighted how hazard exposure and structural vulnerability jointly determine criticality, reinforcing the importance of prioritizing specific highway sections for resilience planning.

Experience from past earthquakes and landslides in the IHR reveals that roads in this region are highly vulnerable (Kumar et al., 2017; HPTCP, 2022; HPSDMA, 2024). Their damage/blockage can significantly impact emergency rescue and recovery operations immediately after such disasters. In addition, road disruptions can hinder reconstruction/repair efforts and other activities during the affected period. For example, in 2023, unprecedented rainfall triggered more than 5500 landslides in the state of Himachal Pradesh, India, resulting in the destruction of thousands of buildings and damage to roads at more than 350 locations (HPSDMA, 2024). Due to road blockages caused by such events, communities in this region have often been cut off for durations ranging from several days to even months (HPSDMA, 2024). In addition to landslides, another potential cause of road blockages during earthquakes is the collapse of buildings constructed adjacent to hilly roads without maintaining the proper offset distance. Moreover, some roads are built next to unsupported and unstable hill cuts or slopes exceeding 3.5 m in height (HPTCP, 2022), often without maintaining the required minimum offset, which increases the risk of slope failure and subsequent blockages. Therefore, it is essential to ensure that hilly roads maintain their functionality to support effective rescue and recovery operations during hazard events. In this context, decision-support tools for managing post-disaster debris removal and sequencing operations (e.g., Lorca et al., 2015; Kim et al., 2018; Tabata et al., 2019) demonstrate how optimizing debris clearance can significantly reduce recovery delays and improve network functionality in disaster-affected areas. However, these studies have been developed largely for plain regions, and equivalent approaches that account for the complex topography and unique challenges of hilly regions are still limited.

Further, a significant number of studies have focused on the seismic and landslide vulnerability assessment of buildings in this region (e.g., Surana et al., 2018; Aggarwal et al., 2024; Raj et al., 2024; Kulariya and Saha, 2024a; 2024b; Kulariya et al., 2026). In addition, a few studies such as Malama et al. (2025) have proposed frameworks to assess earthquake-induced landslide risk for transportation networks in hilly regions. However, a comprehensive methodology that simultaneously considers both earthquake-induced building debris and earthquake-induced landslide debris, while accounting for the region-specific characteristics of the IHR, is yet to be developed. Therefore, it is crucial to propose methodologies that, in the case of pre-disaster scenarios, identify vulnerable road segments and compare potential blockage scenarios across different segments. In the case of post-disaster scenarios, the methodology should estimate the functional recovery time of affected roads under various hazard scenarios to facilitate resource allocation and prompt road recovery.

This study aims to address the aforementioned research gaps in assessing the functional recovery of hilly roads located in the IHR. The specific objectives of the study are (a) to develop a methodology for identifying critical road segments prior to natural hazard events, thereby enabling targeted disaster mitigation activities and strengthening measures to minimize road blockages during earthquakes and earthquake-induced landslides, (b) to gather expert estimates on the time required to clear building and landslide debris from affected road segments, supporting post-disaster recovery planning, and (c) to demonstrate the application of the collected recovery data in post-disaster scenarios through a hypothetical case study. The findings from this study can aid in formulating effective mitigation strategies and guiding resource allocation for roads in the IHR under earthquakes and earthquake-induced landslides.

2. Methodologies for identification of critical road segments and assessing expected functional recovery of roads in hilly regions

Methodologies for identifying the critical road segments and assessing their expected functional recovery time (T_r) under earthquake and earthquake-induced landslide scenarios are presented herein. These are structured into steps corresponding to pre-hazard (Fig. 1) and post-hazard scenarios (Fig. 2). The pre-hazard scenario focuses on identifying critical road segments prior to natural hazard events, while the post-hazard scenario addresses recovery assessment once damage has occurred. In the case of a pre-hazard scenario, the following steps are to be followed.

a) Select the study area and identify key nodes such as road intersections, hospitals, public works department (PWD) offices, educational institutions, emergency shelters, community centers, etc. The selection of nodes primarily depends on the objectives of the study, whether it is to assess the access to healthcare facilities or other essential services, evaluate connectivity to the nearest emergency shelters, or plan future resource and machinery allocations to ensure smooth post-disaster recovery, or a combination of these objectives.

b) Identify the potential factors that may cause blockages along the road segment during an earthquake event, such as vulnerable buildings, active-landslide sites, slow-moving landslide sites, and unsupported hill cuts. Rapid visual screening techniques can then be employed to assess the seismic vulnerability of roadside buildings and determine those likely to collapse during an earthquake. Suppose, x buildings are located between two nodes under consideration, and the roadside width of each building is denoted by L_{B_1}, L_{B_2}, … L_{B_i}, …. L_{B_x}. A coefficient termed the blockage factor, $B_B \in \{0,1\}$, can then be assigned to each building based on its perceived vulnerability. While assigning the blockage factor, considerations should include the offset distance between the building and the road, the ratio of building height to this offset, and other geometric or structural factors that influence the potential of falling debris to obstruct the roadway. The total length of road susceptible to blockage by building debris can then be calculated as:

$$\widetilde{L}_b = \sum_{i=1}^{x} B_{B_i} L_{B_i} \tag{1}$$

where, B_{B_i} = blockage factor corresponding to i^{th} building.

c) To further refine the estimate of road susceptibility to blockage by building debris, fragility assessments can be performed for the surveyed buildings or for archetype buildings representative of the region. This approach allows state-dependent blockage factors to be incorporated. Let $P(DS_y|IM = im, building = i)$ denote the probability that i^{th} building attains damage state DS_y (defined in terms of an engineering demand parameter, EDP) at intensity measure $IM = im$, then the $\widetilde{L}_b$ can be calculated as:

$$\widetilde{L}_b = \sum_{i=1}^{x} L_{B_i} \left[\sum_{y=1}^{z} P(DS_y|IM = im, building = i) \overline{B}_y \right] \tag{2}$$

where, $\overline{B}_y$ = mean blockage factor associated with the DS_y damage state, and z = total number of damage states. The value of $P(DS_y|IM = im, building = i)$ can be computed as:

For DS_z: $P(DS_z|IM = im, building = i) = P(EDP \geq edp_z|IM = im,$

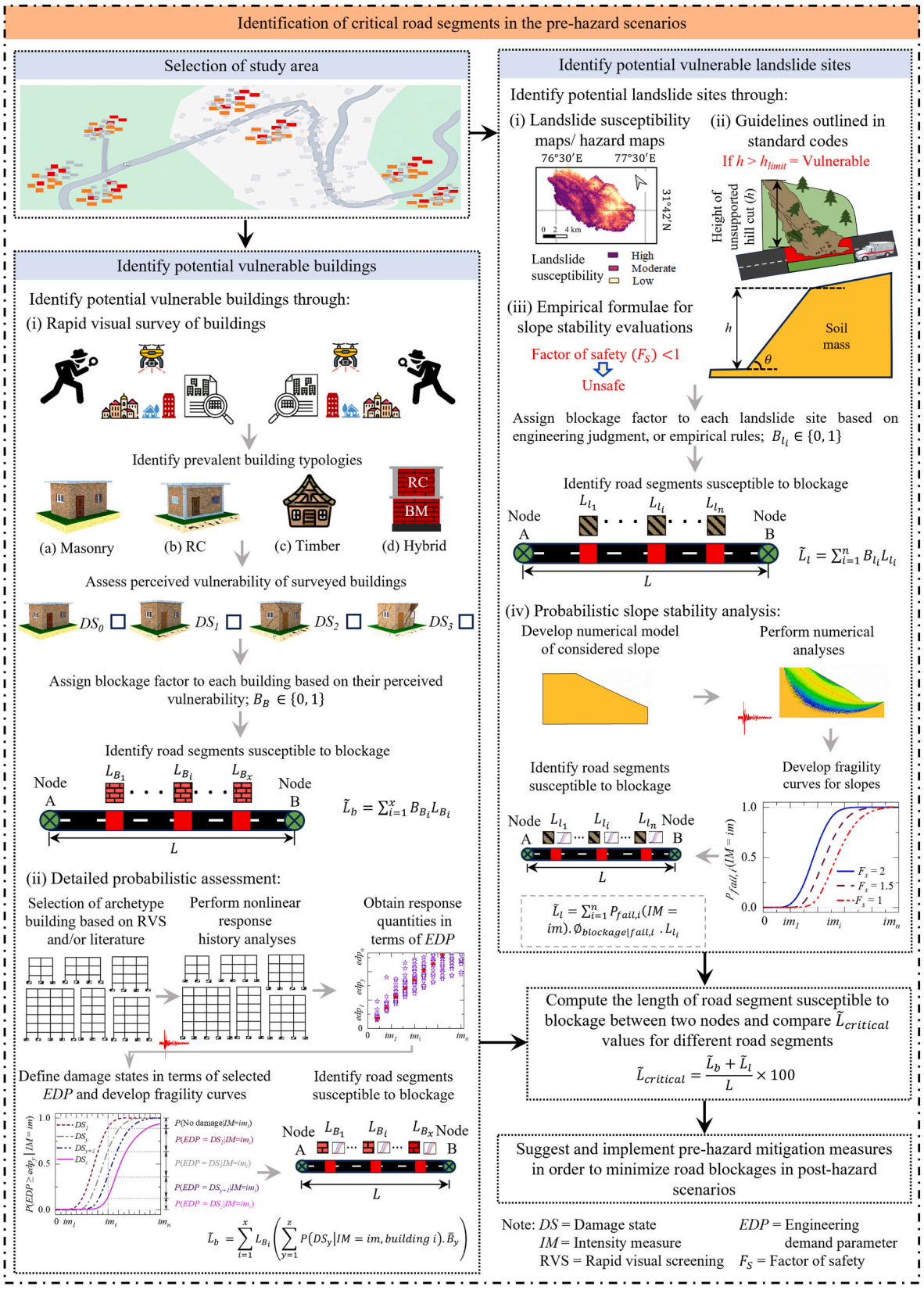


Fig. 1. Methodology for identifying critical road segments in pre-hazard scenarios.

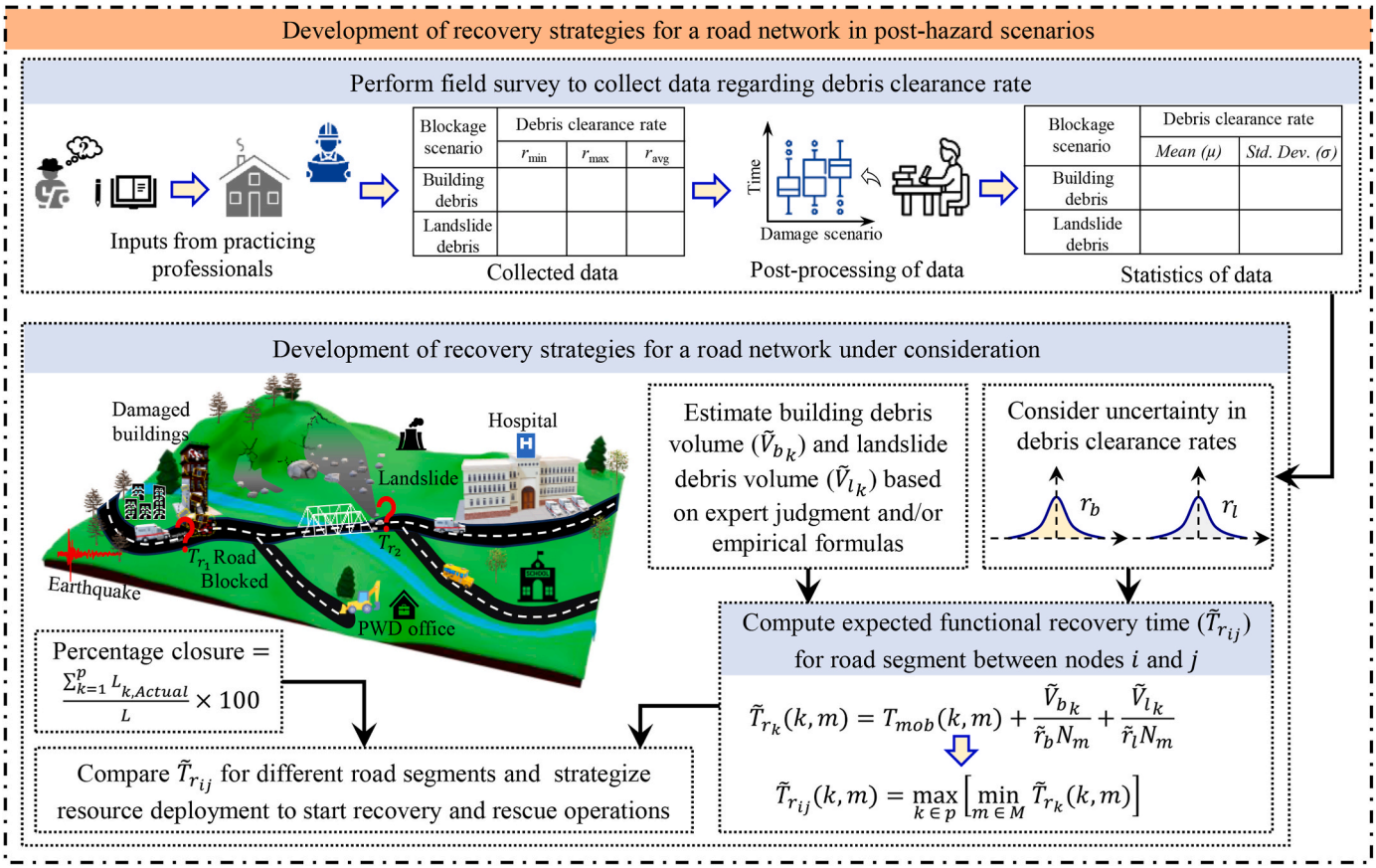


Fig. 2. Methodology to compute expected functional recovery time of a road in post-hazard scenarios.

$building = i\big)$

$$\text{Else}: P\left(DS_y \middle| IM = im, building = i\right) = P\left(EDP \geq edp_y \middle| IM = im, building = i\right) - P\left(EDP \geq edp_{y+1} \middle| IM = im, building = i\right) \quad (3)$$

This formulation enables the blockage factor to be represented not only as binary (0 or 1) but also as a weighted average across possible damage states. In cases where information on state-dependent blockage factors is unavailable, $\overline{B}_y \in [0,1]$ can be assumed using engineering judgment or values reported in the literature.

d) To compute the length of the road segment likely to be affected by landslides, landslide susceptibility maps, slope stability evaluation techniques, and relevant design guidelines can be employed to identify the potential landslide sites. Suppose there are n landslide-prone or active-landslide sites, and the roadside length of each site is denoted by $L_{l_1}, L_{l_2}, \ldots L_{l_i}, \ldots L_{l_n}$. The total road length susceptible to being blocked by landslide debris can then be computed as:

$$\widetilde{L}_l = \sum_{i=1}^{n} B_{l_i} L_{l_i} \quad (4)$$

where, B_{l_i} = blockage factor corresponding to i^{th} landslide site. In its simplest form, $B_{l_i} \in \{0,1\}$ can be assigned based on whether the slope is judged to have the potential to block the road or not. Such binary assignment may be made using engineering judgment, rapid visual screening techniques, or empirical rules. However, if a detailed probabilistic assessment of i^{th} landslide site is available, the $\widetilde{L}_l$ can be computed more rigorously as a product of three components: (i) the probability of slope failure at $IM = im$, i.e., $P_{fail,i}(IM = im)$, (ii) a conditional blockage fraction $\varnothing_{blockage|fail,i}$ which represents the expected proportion of the road width blocked given a slope failure, and (iii) roadside length of each landslide site L_{l_i}.

$$\widetilde{L}_l = \sum_{i=1}^{n} P_{fail,i}(IM = im).\varnothing_{blockage|fail,i}.L_{l_i} \quad (5)$$

where, $\varnothing_{blockage|fail,i} \in [0,1]$ with 0 representing no blockage, 1 representing complete blockage, and intermediate values corresponding to partial blockages (e.g., one lane obstructed).

e) The percentage length of a road segment between two nodes that is susceptible to blockage, denoted by $\widetilde{L}_{critical}$, can then be computed as:

$$\widetilde{L}_{critical} = \frac{\widetilde{L}_b + \widetilde{L}_l}{L} \times 100 \quad (6)$$

where, L = total length of the road between two nodes. Road segments can be compared based on their $\widetilde{L}_{critical}$ values, and areas with higher percentages can be flagged as priority zones for mitigation. This enables proactive planning to minimize road blockages and maintain accessibility during and after natural hazard events. Moreover, post-disaster resources can be strategically pre-positioned in locations that are expected to remain cut off for longer durations, especially if their recovery depends on the functionality of connecting roads and nearby villages, and no resources are currently available in those areas.

In post-hazard scenarios, effective resource allocation and prompt recovery depend on the extent of closure of different road segments due to building and landslide debris. Based on ground reports (e.g., field office, community inputs, etc.), the location and length of road blockages due to building debris ($L_{b,Actual}$) and landslide debris ($L_{l,Actual}$) can be identified. The percentage closure (PC) of a road segment can then be

estimated as the ratio of the blocked length to the total length of the road segment between two nodes.

$$PC = \frac{L_{b,Actual} + L_{l,Actual}}{L} \times 100 \tag{7}$$

However, percentage closure alone is not sufficient to assess recovery in post-hazard situations, as road functionality also depends on the volume of debris to be cleared. The volume of debris can be estimated either through expert judgment, remote sensing data, or using empirical formulas based on field data. The time required to clear debris (hereafter referred to as debris clearance time) is typically estimated based on professional experience or by dividing the debris volume by standard debris removal rates (hereafter referred to as debris clearance rate, in cubic meters per hour) provided by practicing professionals or disaster response agencies. Let T_{r_k} represents the time required to clear the debris volume V_k from the k^{th} blockage along a road segment between nodes i and j containing p blockage locations. Assuming N debris clearance machines are deployed, each with a clearance rate r, the clearance time can be computed as:

$$T_{r_k} = \frac{V_k}{rN} \tag{8}$$

The expected functional recovery time for the road segment between two nodes can then be calculated as:

$$T_{r_{ij}} = \sum_{k=1}^{p} T_{r_k} \tag{9}$$

In practice, different clearance rates apply to different types of debris (e.g., earthquake-induced building debris and earthquake-induced landslide debris). Moreover, multiple machines may be mobilized from different locations. To account for this, including mobilization time, Eq. (8) can be generalized as:

$$T_{r_k}(k,m) = T_{mob}(k,m) + \frac{V_{b_k}}{r_b N_m} + \frac{V_{l_k}}{r_l N_m} \tag{10}$$

where, m = index representing the machinery location, $T_{mob}(k,m)$ = mobilization time from the machinery location m to blockage location k, V_{b_k} = volume of earthquake-induced building debris at blockage k, V_{l_k} = volume of landslide debris at blockage k, N_m = number of machines available at location m, and r_b and r_l = debris clearance rates (m^3/hour) for earthquake-induced building debris and landslide debris, respectively.

In reality, debris volumes, clearance rates, and mobilization times are uncertain due to variability in hazard severity, site accessibility, and resource availability. To incorporate uncertainty, the deterministic variables are replaced with random variables that capture the inherent variability in debris generation and clearance processes. The building debris volume, $\widetilde{V}_{b_k}$, is uncertain due of damaged buildings that actually contribute to the blockage. Similarly, the landslide debris volume, $\widetilde{V}_{l_k}$, is uncertain due to variability in slope geometry, soil properties, failure depth, runout distance, and other parameters required for estimating the volume of displaced material. The clearance rates for building and landslide debris, denoted by $\widetilde{r}_b$ and $\widetilde{r}_l$, are represented as random variables to account for variability in machinery capacity, operator efficiency, and the nature of the debris being cleared. In the absence of detailed information, these rates can be modeled using truncated normal distributions, i.e., $\widetilde{r}_b, \widetilde{r}_l \sim max\{0, N(\mu, \sigma^2)\}$. The mobilization time, $T_{mob}(k,m)$, is also uncertain and may be represented as a discrete or continuous random variable depending on road accessibility, traffic conditions, and resource availability. It should be noted that any of these uncertain parameters, i.e., debris volumes, clearance rates, or mobilization times, may follow distributional forms such as normal, lognormal, Weibull, uniform, etc., if supported by empirical data or expert judgment (e.g., Çelik et al., 2015; Sayarshad et al., 2020; Ma et al., 2022; Tian et al., 2024). The stochastic clearance time is therefore expressed as:

$$\widetilde{T}_{r_k}(k,m) = T_{mob}(k,m) + \frac{\widetilde{V}_{b_k}}{\widetilde{r}_b N_m} + \frac{\widetilde{V}_{l_k}}{\widetilde{r}_l N_m} \tag{11}$$

Thus, the clearance time calculated from Eq. (11) captures the variability of debris generation and clearance processes and allows estimation of expected recovery times and their probability distribution.

When debris clearance machinery can be deployed from multiple locations, both mobilization time and debris clearance time must be considered together. For each blockage, the optimal machinery location is the one (out of M potential location of machinery in the network) that minimizes the total clearance time. However, for any given road segment, traffic can only pass once all blockages are cleared. Therefore, the functional recovery time for a segment is governed by the slowest (i.e., maximum over k) among these optimal debris clearance times. In other words, the functional recovery time of a road segment between nodes i and j with blockages $k \in p$ can be obtained as:

$$\widetilde{T}_{r_{ij}}(k,m) = \max_{k \in p}\left[\min_{m \in M} \widetilde{T}_{r_k}(k,m)\right] \tag{12}$$

The calculated $\widetilde{T}_{r_{ij}}$ values for all road segments can be compared to identify those with longer recovery times. Segments with higher $\widetilde{T}_{r_{ij}}$ values indicate potential bottlenecks in network restoration. By analyzing these values, resources can be allocated strategically to reduce the longest recovery times, promoting a more balanced and synchronized restoration across the network. This prevents situations where certain segments receive abundant resources and are restored quickly, while others remain inaccessible for extended periods. To support such prioritization, methods such as the Critical Path Method (Lavelle et al., 2020), Monte Carlo simulation (Aydin et al., 2018; Dong et al., 2022; Fang et al., 2022), and other optimization techniques (Zhang and Miller-Hooks, 2015; Gokalp et al., 2021) can be employed. These approaches help to identify critical road segments, assess uncertainties in restoration times, and develop robust deployment schedules that minimize total network recovery duration. The implementation of the proposed methodologies is further illustrated through a case study conducted for hilly roads situated in the IHR and presented in the subsequent sections.

3. Case study

To demonstrate the application of the proposed methodologies, a detailed field study was conducted on a section of the Mandi-Bajaura Road in the Mandi region of Himachal Pradesh, India, which falls under seismic Zone-V as per the Indian standard for earthquake resistant design, i.e., IS1893 Part 1 (BIS, 2016). The selected case study route connects the Indian Institute of Technology Mandi (IIT Mandi) to the Zonal Hospital Mandi, a major healthcare facility serving the region. This road plays a vital role in the regional transportation network, linking educational institutions, healthcare facilities, and nearby villages, thereby enabling communities to access essential services and carry out daily household activities. The selected road section is a part of Major District Road 23 (MDR23), which also serves as a critical feeder route to Kullu district, particularly during blockages on National Highway 3 (NH3). In this study, road intersections, hospitals, and villages along the road were selected as nodes. The Zonal Hospital Mandi and IIT Mandi (North Campus) were chosen as the two terminal nodes, marking the start (Node 1) and end point (Node 11) of the selected portion of road, as shown in Fig. 3. In addition to the terminal nodes, nine intermediate nodes were identified based on their geographic location and contextual importance along the route, bringing the total to eleven nodes. The importance of each road segment was evaluated based on several key factors, including the number of villages it connects, its topological significance, its susceptibility to becoming unusable due to building collapse, and its role in providing access to medical services for

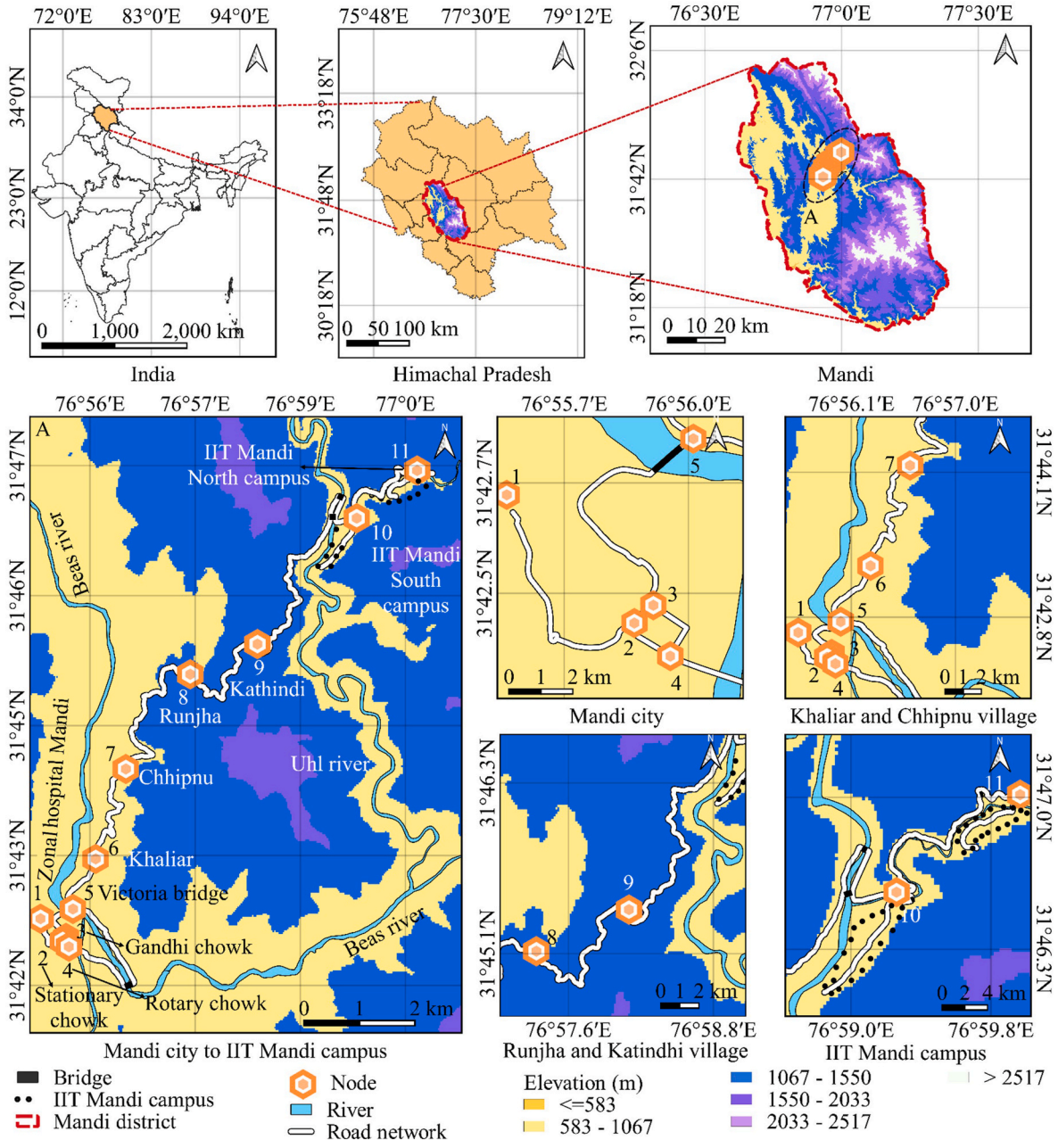


Fig. 3. Location of case study area and selected nodes.

various demographic groups. Moreover, multiple village roads are connected to MDR23, with the majority of the communities residing between Node 5 and Node 11 as shown in Fig. 3. Therefore, the present study focuses on this representative segment of MDR23, specifically between Node 5 and Node 11, to demonstrate the applicability of the proposed methodologies. Additionally, the survey identified critical infrastructure points such as community health centers, educational institutions, and PWD offices to support the prioritization and systematic initiation of post-disaster rescue and recovery operations. These nodes divided the considered road into smaller sections, as schematically shown in Fig. 3, which helped in systematically recording field observations during the survey and facilitated the identification of vulnerable portions of the road between the nodes. Further details of the survey are presented in the subsequent section.

3.1. Identification of vulnerable buildings along the considered road

A comprehensive Rapid Visual Screening (RVS) survey was carried out to determine the location and characteristics of existing buildings along the selected road, following the guidelines outlined in Kulariya et al. (2024a) and NDMA (2020). Due to challenging topographical conditions, including limited visibility, dense vegetation cover, and accessibility constraints, other forms of survey such as drone-based aerial surveys and satellite imagery, were not feasible in the study region. Therefore, in the present study, assessment was conducted entirely through ground-based RVS. Through this RVS, a total of 523 buildings were surveyed along the selected road, and the location of survey buildings is shown in Fig. 4.

The surveyed buildings were categorized based on occupancy types, which include residential with commercial, residential, commercial, government, educational, healthcare, and other. The percentage distribution of these buildings according to occupancy type is presented in

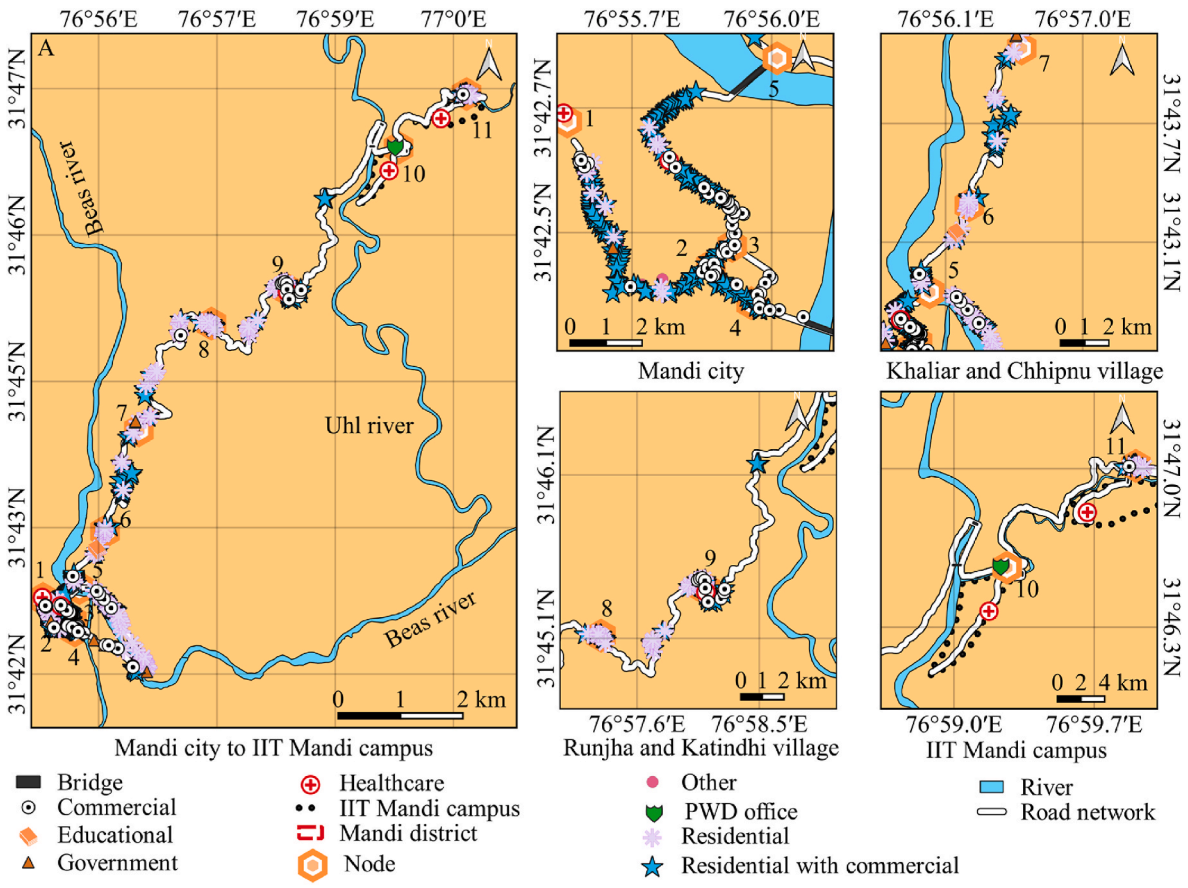


Fig. 4. Location of nodes and surveyed buildings in the case study area.

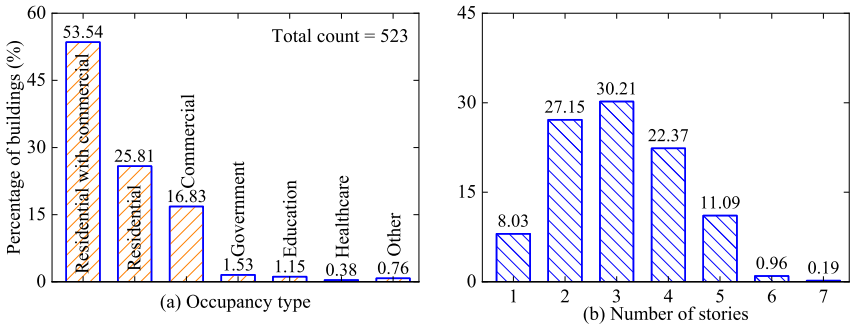


Fig. 5. Distribution of surveyed buildings in the study area with respect to (a) occupancy type, and (b) number of stories.

Fig. 5(a). It can be noted that the majority of the surveyed buildings are either residential with commercial (53.54 %) or purely residential (25.81 %). In this context, residential with commercial buildings refer to buildings that allocate a part of the building, typically the floor closest to the access road, for commercial use (Aggarwal et al., 2024). Fig. 5(b) presents the percentage distribution of surveyed buildings with respect to the number of stories. It can be observed from Fig. 5(b) that 3-story buildings represent the highest proportion, accounting for 30.21 %, followed by 2-story and 4-story buildings at 27.15 % and 22.37 %, respectively.

Further, in this RVS survey, it was observed that the surveyed building stock comprises various typologies, including reinforced concrete (RC), brick masonry (BM), stone masonry (SM), hybrid buildings constructed with more than one material (RC + BM, RC + SM, BM + SM), and traditional wooden buildings. Among the 523 surveyed buildings, the numbers of RC, BM, SM, RC + BM, RC + SM, BM + SM, and traditional wooden buildings were 356, 58, 32, 12, 8, 31, and 26, respectively. It is worth noting that during the RVS, significant emphasis was placed on identifying vulnerability attributes known to impact the seismic performance of buildings. These included susceptibility to pounding (SP) due to insufficient seismic gap, soft story (SS), heavy overhang (HO), absence of framing action (AFA), and setback (SetB), among others. Fig. 6 presents representative illustrations of selected vulnerability attributes as observed during the field survey.

The distribution of these attributes across different typologies is summarized in Fig. 7. Among the considered attributes, susceptibility to pounding due to insufficient seismic gap and the presence of a soft story were the most commonly observed in the surveyed buildings. Susceptibility to pounding was assessed using FEMA P154, 2003 criteria, which consider factors such as insufficient separation between adjacent



Fig. 6. Examples of vulnerability attributes present in surveyed buildings.

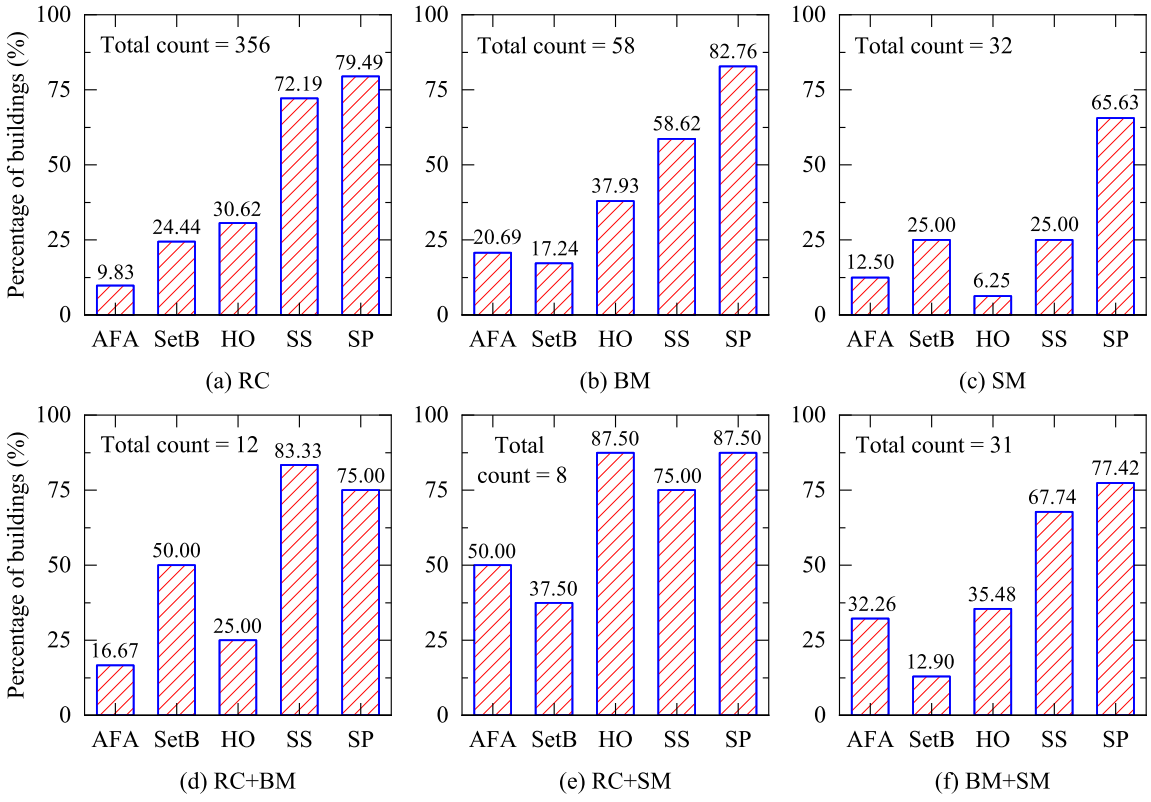


Fig. 7. Distribution of various vulnerability attributes across different building typologies.

buildings, vertical offsets in floor levels greater than two feet, and height differences exceeding two stories. This attribute was present in 79.49 % of RC, 82.76 % of BM, 65.63 % of SM, 75.00 % of RC + BM, 87.50 % of RC + SM, and 77.42 % of BM + SM buildings. The presence of soft story attribute was identified based on the criteria outlined in IS 1893 Part 1 (BIS, 2016), which defines a soft story as a floor with a significant

reduction in lateral stiffness typically due to open stories or missing infill walls at that level. This attribute was present in 72.19 % of RC, 58.62 % of BM, 25.00 % of SM, 83.33 % of RC + BM, 75.00 % of RC + SM, and 67.74 % of BM + SM buildings.

The presence of heavy overhangs, identified in accordance with FEMA P154, 2003, was observed in 37.93 % of BM, 87.50 % of RC + SM, and 35.48 % of BM + SM buildings, while in the remaining building typologies, it was about 30 % or less. Absence of framing action attribute was identified where continuity in the load-resisting system was interrupted, either through misalignment of columns or missing structural members. This attribute was prevalent in 50 % of RC + SM, 32.26 % of BM + SM, and 20.69 % of BM buildings. The setback attribute, identified based on the criteria outlined in IS 1893 Part 1 (BIS, 2016), was observed in 50 % of RC + BM, 37.50 % of RC + SM, and about 25 % of RC and SM buildings.

Further, to identify vulnerable RC buildings, the methodology proposed by Kulariya et al. (2024a) was applied, where the obtained final score was compared with the Expected Multi-Hazard Vulnerability Score (EMHVS) thresholds provided in Table 1 (Kulariya et al., 2024a) to determine the corresponding damage states (DS_z).

For masonry buildings and traditional wooden buildings, the pre-earthquake rapid visual screening was carried out following the guidelines provided by NDMA (2020), which classify buildings into green, yellow, or red tags. Each tag is associated with a specific set of conditions related to structural configuration, architectural features, soil and foundation conditions, and siting issues. A green-tagged building is expected to sustain no visible damage during an earthquake and remain fully functional. However, since tagging is based on pre-earthquake rapid visual screening, such buildings may still experience damage depending on the earthquake intensity and are therefore assumed to be in DS_1. A red-tagged building is classified as unsafe for occupancy due to the likelihood of severe structural and/or non-structural damage or serious siting issues, which may render the building unusable. As such, red-tagged buildings are considered equivalent to buildings classified under the DS_3 damage state using the methodology proposed by Kulariya et al. (2024a). A yellow-tagged building is expected to experience moderate damage and is deemed useable with temporary interventions. Accordingly, yellow-tagged buildings are considered equivalent to buildings with DS_2. It should be noted that, in the absence of dedicated RVS guidelines for hybrid buildings comprising both reinforced concrete and masonry, such buildings are assessed using both the methodologies proposed by Kulariya et al. (2024a) and NDMA (2020). The higher damage state obtained from either of the two is then assigned to the building. The distribution of surveyed buildings across the expected damage states is presented in Fig. 8. It can be observed that, out of the 523 buildings surveyed, 212 fall under DS_3, 235 under DS_2, and 76 under DS_1.

Fig. 9 shows the locations of buildings classified under DS_3 situated between various nodes along the selected road, highlighting their potential to obstruct road access during or after an earthquake. In this study, the length of road susceptible to blockage is calculated by multiplying the width of each building along the roadside (L_{B_i}) with a blockage factor (B_{B_i}), as discussed in the methodology section. Due to the unavailability of blockage data for roadside buildings in the Indian Himalayan Region during earthquakes, a conservative assumption of B_{B_i} equal to 1 is adopted for buildings in DS_3, implying that the full width of each building could potentially block the road. For buildings categorized under DS_1 and DS_2, B_{B_i} is assumed to be 0, indicating no road blockage contribution in these lower damage states. Fig. 9 also shows the location of potential landslide sites, which is discussed in the subsequent subsection. The survey also identified five medical centers, including the Zonal healthcare facility (denoted as Node 1 in Fig. 3) in Mandi city, which are likely to play a vital role in emergencies. In addition, two PWD offices located near the Zonal Hospital Mandi and IIT Mandi South Campus were identified during the survey. These offices can serve as potential centers for initiating rescue and recovery operations in the post-disaster phase. This information is further utilized in a subsequent section to calculate the critical length of the road between the considered nodes.

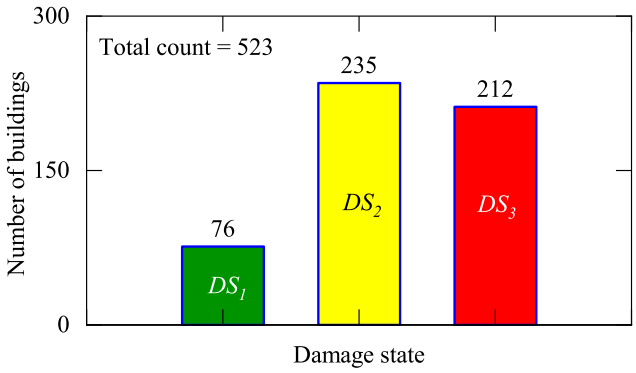


Fig. 8. Distribution of surveyed buildings with respect to expected damage state.

3.2. Identification of potential landslide sites along the considered road

During the survey, potential landslide sites along the considered road were identified using multiple criteria. The first criterion follows the guidelines outlined in HPTCP (2022), which consider unsupported hill cuts exceeding 3.5 m in height as vulnerable to landslides. While this criterion is crude and may not portray the complete landslide susceptibility of a site, it serves as an effective initial screening method in the absence of detailed geotechnical data. When more accurate and site-specific information becomes available for the entire road segment, such preliminary criteria can be refined or replaced. Fig. 10 shows examples of typical unsupported slopes observed during the field survey that exceed the 3.5 m threshold. Using this criterion, a total of 20 potential landslide-prone sites were identified in the study area. It should be noted that these locations include only uphill-side landslide-prone sites along the road. Potential downhill-side landslide sites that could cause complete road damage were not considered in the present study.

Further, in the second criterion, the factor of safety (F_s) for the unsupported hill cut/potential landslide sites are calculated, using the empirical formula given by Pack et al. (1998) as follows:

Table 1
EMHVS corresponding to different damage states.

EMHVS	Damage state	Description
EMHVS >88	No damage	No damage
88 ≥ EMHVS >78	DS_1	Slight damage to infill walls
78 ≥ EMHVS >63	DS_2	Moderate structural damage and heavy non-structural damages
EMHVS ≤63	DS_3	Heavy structural damage with wall failures and partial roof/floor collapse

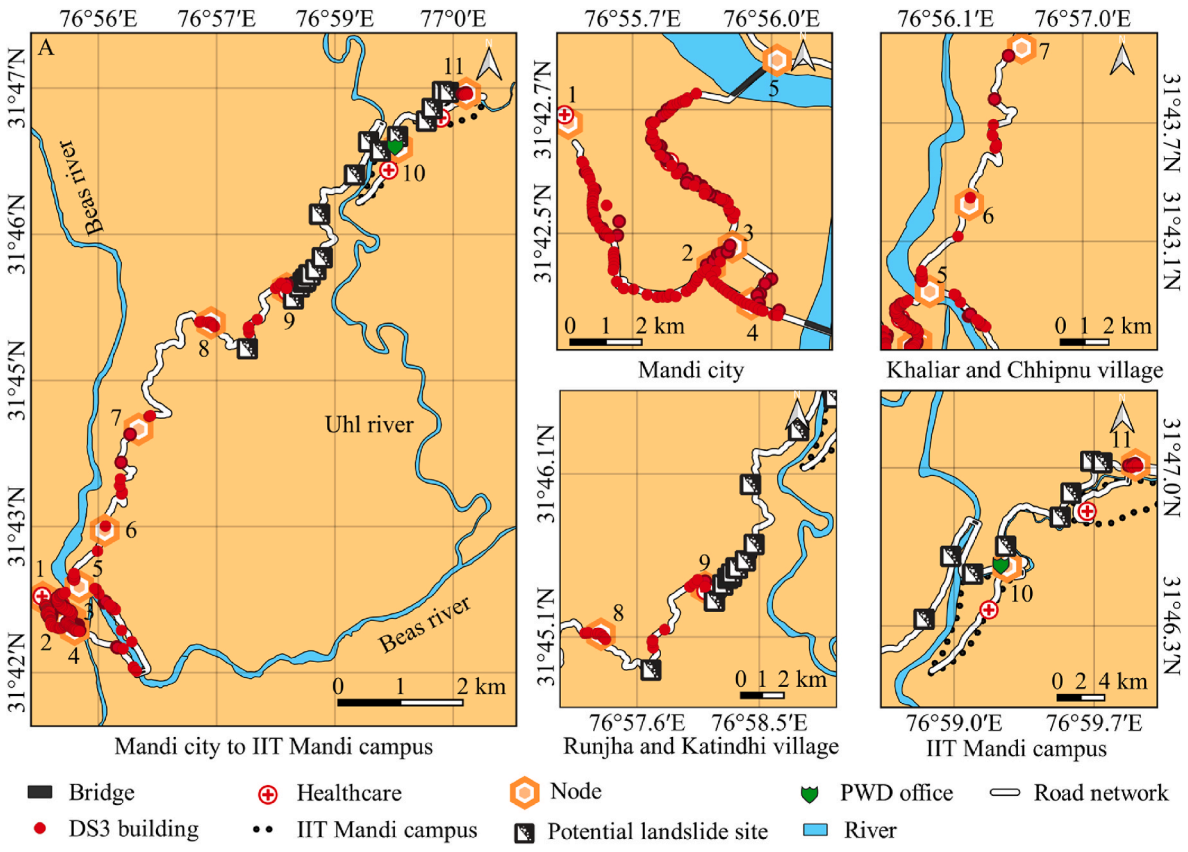


Fig. 9. Vulnerable buildings (DS_3) and landslide sites along the considered road.

$$F_s = \frac{\frac{C_s}{\rho_s g h_s} + \cos\theta\left[1 - C_w\frac{\rho_w}{\rho_s}\right]\tan\varnothing_f}{\sin\theta} \tag{13}$$

where, C_s, ρ_s, $\varnothing_f$, c_w , ρ_w, θ, and g denote the cohesion, average soil density, internal friction angle of soil, relative wetness, unit weight of water, slope angle, and acceleration due to gravity, respectively. The soil thickness h_s represents the potential failure depth. As per this criterion, $F_s = 2$ indicates a safe/stable slope, $F_s = 1.5$ indicates a slope critical to failure, and $F_s < 1$ indicates an unsafe/unstable slope.

In the absence of detailed geotechnical investigations for individual slopes, the values of the required input parameters are assumed based on the existing database of laboratory tests conducted for active-landslide sites in the study region. The uncertainties in these input variables are incorporated through their probabilistic distributions. The parameter ρ_s is assumed to follow a lognormal distribution with a mean value of 1845 kg/m^3 and a coefficient of variation (COV) of 7.09 %, while the $\varnothing_f$ is taken as 25° with a COV of 5 %. The variables C_s and h_s are modeled as truncated normal distributions, with mean values of 5.36 kPa (COV = 60.79 %) and 5 m (standard deviation = 1.65), respectively. The variable c_w is modeled as uniformly distributed in the range of 0 and 1. These values are assumed based on the reported range of these parameters in Kulariya et al. (2024b) and Devi et al. (2022). The mean value of θ is obtained from Google Earth (GE, 2025) corresponding to the coordinates of landslide sites and vulnerable hill cuts identified during the field survey. The parameter θ is assumed to follow a normal distribution with a COV of 10 %, based on the observation that the minimum and maximum slope angles from Google Earth typically deviate by about 10 % from the median value. Further, the ρ_w is considered to be 1000 kg/m^3, and the acceleration due to gravity is taken as 9.81 m/s^2.

For each considered site, 100000 realizations of the input variables C_s, ρ_s, $\varnothing_f$, c_w and θ are generated through Monte Carlo simulation based on their prescribed statistical distributions. For every realization, the factor of safety is then computed using Eq. (13). The probability of failure for each site is then estimated as

$$P_{fail}\left(F_s \le F_{s,threshold}\right) = \frac{n_{fail}}{n_{total}} \tag{14}$$

where, n_{fail} = number of simulations resulting in $F_s \le F_{s,threshold}$, and n_{total} = total number of simulations performed for each site. The obtained values of $P_{fail}\left(F_s \le F_{s,threshold}\right)$ are presented in Table 2. It can be observed that none of the sites can be classified as safe since the probability of achieving ($F_s \ge 2$) is zero across all locations. This highlights the overall vulnerability of the study area to slope failures.

Among the 20 sites, a clear distinction is observed between unstable and critical slopes. Sites with slope angles exceeding 36° (e.g., LS1, LS8, LS9, LS10, LS13, LS14, LS15, LS16, and LS18) show the $P_{fail}(F_s < 1)$ equal to 1.0, confirming that these steep slopes are unsafe under all uncertain scenarios considered for the input variables. In addition, sites with moderate slope angles between 26° and 35° (e.g., LS3, LS4, LS5, LS7, LS11, LS12, and LS19) also fall into the unsafe category, with $P_{fail}(F_s < 1)$ values between 0.94 and 0.99. It is noteworthy that even relatively gentle slopes (21°–22°; LS2, LS6, LS17, and LS20) exhibit the $P_{fail}(F_s < 1)$ values ranging from 0.67 to 0.75 and $P_{fail}(F_s \le 1.5)$ values between 0.25 and 0.33. This indicates that low-angle slopes in this region are also not inherently stable.

Further, the total length susceptible to blockage ($\widetilde{L_l}$) is computed using Eq. (5), as described in the methodology section. The first component of Eq. (5), i.e., $P_{fail,i}$, representing the probability of slope failure at the i^{th} landslide site, is obtained from Table 2. The second component, $\varnothing_{blockage|fail,i}$, which represents the expected proportion of the road width blocked given a slope fail, is taken as 1. This is because most roads in the study area are single-lane (HPSDMA, 2024), with an average width of 3.5 m, so even a small debris fall can completely obstruct the roadway. The third component (L_{l_i}), represents the road

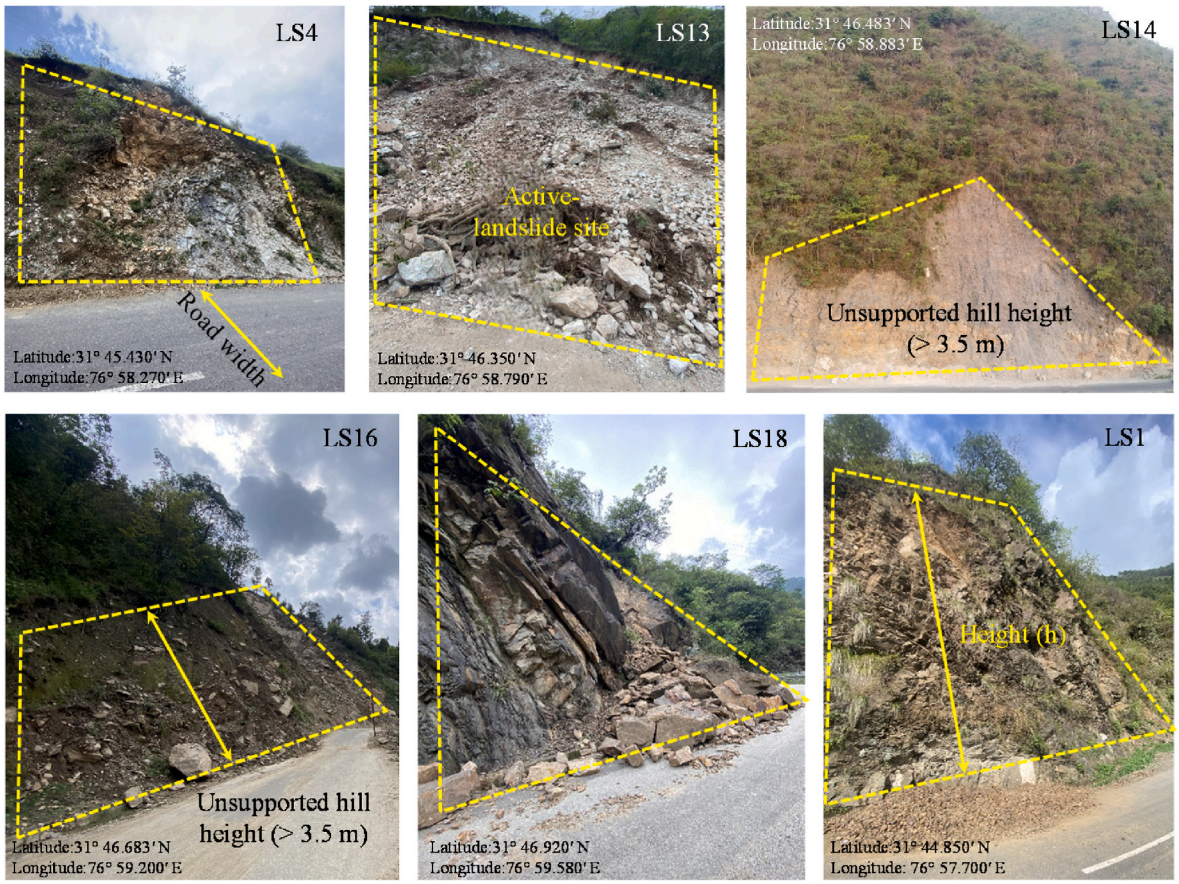


Fig. 10. An example of the unsupported hill cuts is presented along the roadside.

side length of i^{th} landslide site, and is obtained from the field observations.

The locations of these potential landslide sites along the considered road are previously shown in Fig. 9. Notably, the lack of fully stable slopes highlights the region's high susceptibility to landslides, particularly under triggering conditions such as intense rainfall or seismic activity, which could result in road blockages. As observed from Fig. 9, the majority of both vulnerable buildings and potential landslide sites are concentrated between Node 1 to Node 5 and Node 9 to Node 11, respectively. In the subsequent section, a detailed computation is presented to evaluate the critical road lengths between these specified nodes. This analysis is aimed at identifying the most critical road segments based on the spatial distribution of vulnerable buildings and potential landslide sites.

3.3. Identification of critical road segments in the pre-hazard scenarios

In the present study, critical road segments are identified using the methodology described in Section 2. The critical length between two nodes is evaluated by comparing the total road length between the nodes with the portion potentially obstructed by building debris and/or landslide debris. It is assumed that road blockage may occur along the measured lengths of buildings and landslide-prone sites adjacent to the road, as documented during the field survey. The locations of these vulnerable segments are illustrated in Fig. 11. In addition, Table 3 provides the percentage of road length susceptible to blockage, which serves as the primary criterion for assessing the severity and criticality of each road segment. From Table 3, it is evident that the surveyed road segments exhibit varying degrees of susceptibility to blockage due to landslide or building debris. For instance, the segments from Node 4 to Node 5 and Node 6 through Node 9 exhibit relatively low blockage potential, with $L_{critical}$ values less than 10 %. Whereas the segments from Node 5 to Node 6, Node 9 through Node 11 show moderate susceptibility, with $L_{critical}$ values of between 10 and 13 %. However, other segments demonstrate significantly higher susceptibility with $L_{critical}$ values ranging from approximately 60 %–100 %.

Of particular importance are Nodes 10 and 11, corresponding to IIT Mandi's South Campus (Node 10) and North Campus (Node 11), both of which are equipped with basic medical facilities that can provide initial emergency care. However, access to advanced medical services requires connectivity to Mandi town, where the Zonal Hospital (Node 1) is located. In addition, Node 10 houses a PWD office, which can play a critical role in initiating debris clearance operations in post-disaster scenarios. This makes Node 10 a strategically significant location for launching recovery and emergency response efforts. Ensuring uninterrupted access to and from this node is essential for the efficient planning and implementation of recovery operations, particularly to maintain access to medical services for nearby communities and campus residents. While immediate needs can be addressed at campus facilities, restoring connectivity to Node 1 remains a top priority during major emergencies.

Thus, by using the proposed methodology, potential critical nodes and vulnerable road segments can be systematically identified based on their blockage susceptibility and strategic importance within the network. The parameter $L_{critical}$ serves as a key criterion and can be calculated for each segment. This information can be mapped on a GIS platform to generate easily interpretable visual layers, allowing planners and decision-makers to quickly pinpoint the most critical links in the network by integrating factors such as the availability of emergency services and their role in connecting major population centers. For example, key nodes such as Node 10 and Node 11, which serve both as operational hubs and medical support points, should be flagged in

Table 2
$P_{fail}(F_s \leq F_{s,threshold})$ values for the surveyed landslide sites.

Sr. no.	Coordinates		Slope angle (°)	$P_{fail}(F_s \leq F_{s,threshold})$		
	Latitude (*N*)	Longitude (*E*)		Unsafe	Critical	Safe
LS1	31° 44.850′	76° 57.700′	36	1.00	0.00	0.00
LS2	31° 45.350′	76° 58.233′	22	0.75	0.25	0.00
LS3	31° 45.383′	76° 58.217′	27	0.96	0.04	0.00
LS4	31° 45.430′	76° 58.270′	31	1.00	0.00	0.00
LS5	31° 45.440′	76° 58.290′	26	0.94	0.06	0.00
LS6	31° 45.433′	76° 58.283′	22	0.75	0.25	0.00
LS7	31° 45.483′	76° 58.317′	31	1.00	0.00	0.00
LS8	31° 45.483′	76° 58.333′	36	1.00	0.00	0.00
LS9	31° 45.483′	76° 58.333′	37	1.00	0.00	0.00
LS10	31° 45.540′	76° 58.400′	45	1.00	0.00	0.00
LS11	31° 45.617′	76° 58.467′	28	0.98	0.02	0.00
LS12	31° 46.000′	76° 58.417′	26	0.94	0.06	0.00
LS13	31° 46.350′	76° 58.790′	38	1.00	0.00	0.00
LS14	31° 46.483′	76° 58.883′	43	1.00	0.00	0.00
LS15	31° 46.550′	76° 58.920′	51	1.00	0.00	0.00
LS16	31° 46.683′	76° 59.200′	38	1.00	0.00	0.00
LS17	31° 46.800′	76° 59.517′	21	0.67	0.33	0.00
LS18	31° 46.920′	76° 59.580′	36	1.00	0.00	0.00
LS19	31° 47.060′	76° 59.700′	30	0.99	0.01	0.00
LS20	31° 47.050′	76° 59.733′	21	0.67	0.33	0.00

emergency operation plans with clear protocols for ensuring accessibility under different hazard scenarios. Regular field inspections can be used to update observations for these nodes and adjacent segments, ensuring that the vulnerability map (e.g., Fig. 11) remains updated. This method of prioritization, supported by regional vulnerability maps, would enable agencies to pre-position resources and develop targeted response strategies for different scenarios. Further pre-hazard mitigation measures for the identified vulnerable buildings and landslide-prone areas should be adopted, such as maintaining a minimum offset between buildings and the road, and ensuring a minimum height for unsupported cuts, as outlined in the standard guidelines for hilly regions (HPTCP, 2022; Robson et al., 2022, 2025). By adopting such measures, the potential impact of disruptions can be minimized, and recovery operations can be executed more efficiently, thereby improving the overall resilience of the road network.

4. Development of recovery strategies for a road network in post-hazard scenarios

In the post-hazard scenario, restoring connectivity to isolated regions should be the highest priority to ensure the resumption of essential services. To achieve this, information on debris clearance time is critical for planning and deploying the necessary resources on the affected site, such as backhoe loaders or other required equipment. Therefore, the debris clearance time data for the considered road were collected using the procedure outlined in the methodology presented in Fig. 2.

In this study, debris clearance rates (debris volume removed per hour) were obtained from practicing professionals in Himachal Pradesh, India, for both earthquake-induced building debris and landslide debris. In this context, the earthquake was considered the primary hazard, while the landslide was considered as the secondary hazard. It was further assumed that the landslide debris would not impact any building and would only result in road blockages. For each debris scenario, the professionals provided the maximum and minimum volumes they could typically remove per hour based on their field experience in the case study region. It was explained to the professionals that one backhoe loader would be available on-site to remove both building and landslide debris, as is typically the case in hilly regions. A total of 56 responses were collected from Junior Engineers, Assistant Engineers, and Executive Engineers working in the Public Works Department of Himachal Pradesh. These engineers are regularly involved in planning and execution of debris clearance operations within the case study region. Box-and-whisker plots of the average clearance rate (average of the maximum and minimum volumes removed per hour reported) were developed to identify potential outliers. The dataset, after removing these outliers, is shown in Fig. 12 along with the mean (μ) and COV. These rates can be used to estimate debris clearance time for any blockage scenario under consideration.

Further, to illustrate the application of the debris clearance rates, a hypothetical post-hazard scenario was considered. In this scenario, all buildings assessed to be in DS_3 are assumed to have collapsed during the earthquake. The debris volume obstructing the road from each building is estimated as a fraction of its gross building volume, which is calculated as the product of the building's length, width, and height. The building debris volume (denoted as $\widetilde{V}_{b_k}$ in Eq. (11)) is modeled as a uniformly distributed random variable, ranging between 10 % and 20 % of the gross building volume (Argyroudis, 2010; Argyroudis and Pitilakis, 2011). For landslide sites, the length and height measured during field surveys are treated as mean values of truncated normal distributions with a COV of 10 % to account for the uncertainty. The landslide depth is also modeled as a truncated normal distribution with a mean of 5.0 m and a standard deviation of 1.65 m, which ensures that nearly all realizations fall within the plausible range reported in Devi et al. (2022). The landslide debris volume ($\widetilde{V}_{l_k}$) is then computed as the product of the randomly sampled length, height, and depth. Furthermore, the building debris clearance rate ($\widetilde{r}_b$) and landslide debris clearance rate ($\widetilde{r}_l$) are modeled as lognormally distributed variables, with distribution parameters provided in Fig. 12. For each Monte Carlo realization of debris clearance rates, debris clearance times are computed as the ratio of debris volume to the corresponding clearance rate. Let N_r and N_v are the number of realizations of clearance rates and debris volumes, respectively.

$$T_b^{(i,q)} = \sum_{j=1}^{x} \frac{\widetilde{V}_{b\,j}^{(q)}}{\widetilde{r}_b^{(i)}}, T_l^{(i,q)} = \sum_{j=1}^{n} \frac{\widetilde{V}_{l\,j}^{(q)}}{\widetilde{r}_l^{(i)}} \tag{15}$$

$$T_{total}^{(i,q)} = T_b^{(i,q)} + T_l^{(i,q)} \tag{16}$$

where, $T_b^{(i,q)}$ = total clearance time for building debris in a given road segment under the q^{th} debris volume realization and i^{th} clearance rate realization, and $T_l^{(i,q)}$ = total clearance time for landslide debris in the same road segment under the q^{th} debris volume realization and i^{th} clearance rate realization. Further, $i \in \{1, \ldots, N_r\}$ and $q \in \{1, \ldots, N_v\}$ = indices representing the random realizations of clearance rates and debris volumes, respectively, x = number of collapsed buildings in a road segment, n = number of landslide sites in a road segment, $\widetilde{V}_{b\,j}^{(q)}$ = debris volume of j^{th} building under q^{th} debris volume realization, $\widetilde{V}_{l\,j}^{(q)}$ = debris volume of j^{th} landslide site under q^{th} debris volume realization, $\widetilde{r}_b^{(i)}$ = building debris clearance rate under i^{th} realization, and $\widetilde{r}_l^{(i)}$ = landslide debris clearance rate under i^{th} realization. Thereafter, the minimum, maximum, and median debris clearance time in days (d) for each road segment were estimated considering 1000 debris clearance rate and 1000 debris volume (i.e., total 10^6 realizations), and the obtained values are presented in Table 4.

Further, the Critical Path Method was applied to identify the sequence of road segments that would require the maximum clearance time for debris clearance in the selected road network. In this regard, the median debris clearance values from Table 4 are shown in Fig. 13, along with the typical stationed locations of backhoe loaders. The median value was chosen because it represents the central tendency of the observed clearance times and is less sensitive to extreme values than the minimum or maximum, thereby providing a realistic estimate for planning purposes. From Node 1 to Node 5, four possible paths were identified, and the total debris clearance time for each was computed using the values shown in Fig. 13 with a single backhoe loader deployed

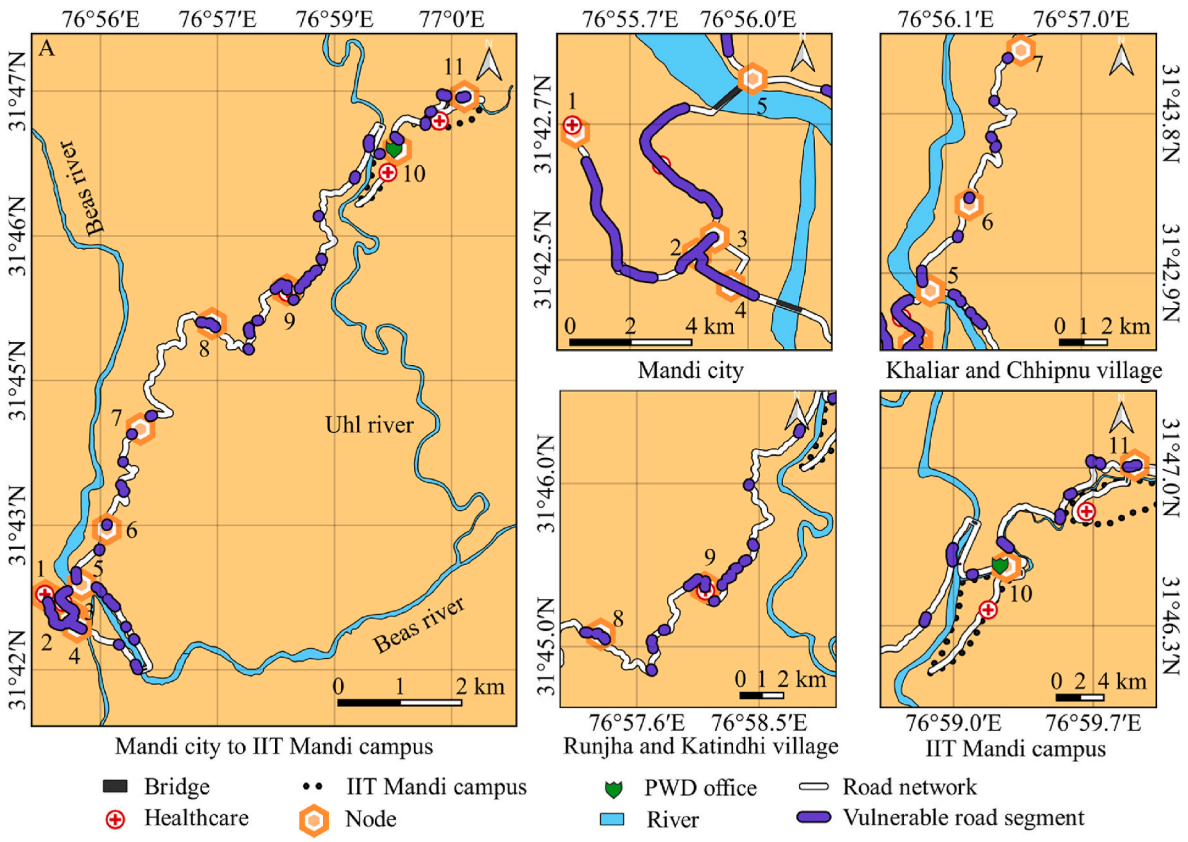


Fig. 11. Map showing the vulnerable road segments along the considered road.

Table 3
Percentage of critical length between different nodes.

Start node	End node	Total length between nodes (m)	Length susceptible to blockage (m) Eq. (1)+ Eq. (5)	Percentage blockage length of road ($L_{critical}$)
Node 1	Node 2	681	542	79.59
Node 2	Node 3	76	76	100.00
Node 3	Node 5	878	535	60.93
Node 2	Node 4	173	173	100.00
Node 4	Node 5	3364	298	8.86
Node 5	Node 6	1158	147	12.69
Node 6	Node 7	2421	65.7	2.71
Node 7	Node 8	3482	102	2.93
Node 8	Node 9	2666	192	7.20
Node 9	Node 10	4279	446	10.42
Node 10	Node 11	2308	266	11.54

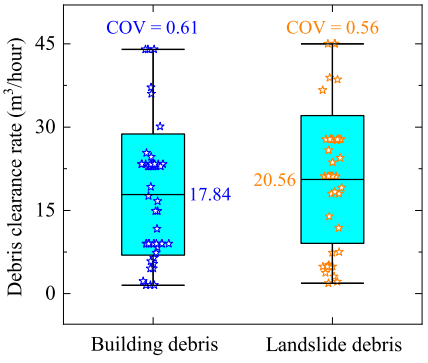


Fig. 12. Box-and-whisker plots of debris clearance rates (after removing outliers) obtained from practicing professionals.

from a single end.

The possible paths and their corresponding total clearance times are:

Path 1: 1 → 2 → 3 → 5 (39.5 d)

Path 2: 1 → 2 → 3 → 4 → 5 (41.8 d)

Path 3: 1 → 2 → 4 → 3 → 5 (47.0 d)

Path 4: 1 → 2 → 4 → 5 (42.1 d)

From Node 5 to Node 11, only one path exists with a total clearance time of 77.2 days. Combining the results, the total debris clearance time for the critical path, i.e., 1 → 2 → 3 → 5 → 6 → 7 → 8 → 9 → 10 → 11, is 116.7 days when one backhoe loader is deployed from a single end. It should be noted that this total clearance time does not account for the mobilization time required to move between blockage locations.

As discussed earlier, two PWD offices are located near Node 1 and Node 10. In the event of an earthquake, backhoe loaders stationed at these locations can be mobilized simultaneously to start clearance op-

Table 4
Debris clearance time for various road segments.

Node *i* - Node *j*	Minimum debris clearance time (d)	Maximum debris clearance time (d)	Median debris clearance time (d)
1–2	17.1	26.3	21.3
2–3	1.2	2.3	1.7
2–4	4.1	7.4	5.6
3–4	2.4	5.3	3.6
3–5	13.2	20.5	16.5
4–5	11.5	19.8	15.2
5–6	3.6	6.8	5.1
6–7	4.6	8.9	6.5
7–8	1.4	2.6	1.9
8–9	3.1	6.1	4.5
9–10	16.6	62.6	36.0
10–11	8.1	45.5	23.2

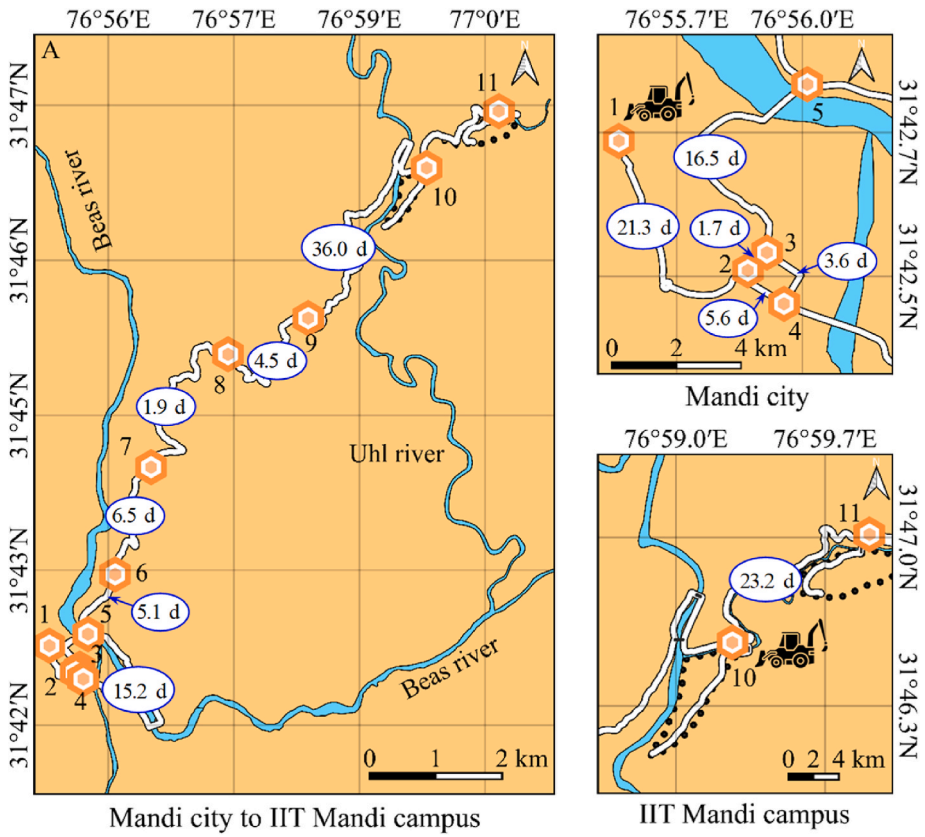


Fig. 13. Median debris clearance time for various road segments and the typical stationed locations of backhoe loaders.

erations from both ends of the critical path. If two identical backhoe loaders start simultaneously at the two ends and work inward without idle time, the expected opening time for the critical path (CP), i.e., $T_r(CP)$, would be:

$$T_r(CP) = \min_{s\in\{1,\ldots,q\}} \max\left(\sum_{ij=1}^{s} T_{r_{ij}} , \sum_{ij=q}^{s+1} T_{r_{ij}} \right) \tag{17}$$

where, q = number of segments in the critical path, $\sum_{ij=1}^{s} T_{r_{ij}}$ = total median debris clearance time taken by the backhoe loader starting at Node 1 to clear road segments 1 through s, $\sum_{ij=q}^{s+1} T_{r_{ij}}$ = total median debris clearance time taken by the backhoe loader starting at Node 10 to clear segments q through $s+1$. Eq. (17) selects the meeting index s that balances the two partial sums as closely as possible, and the larger of the two partial sums of debris clearance times (from the backhoe loader starting at Node 1 and from the one starting at Node 10) represents the time required to open the road along the critical path. It should be noted that the backhoe loader at Node 10 must first clear the road segment between Node 10 and Node 11 to ensure access to the medical facility located at Node 11. This dual-end approach can potentially reduce the effective clearance time, thereby restoring road connectivity to critical services more rapidly. Additionally, if extra backhoe loaders are available, they can be deployed to segments other than those on the critical path to ensure prompt functional recovery of all road segments. Applying Eq. (17) to the critical path above yields $T_r(CP)$ as 59.2 days, with two backhoe loaders deployed at Node 1 and Node 10, and the meeting point would be Node 9. Also, if the backhoe loader operators can split a single segment and work from both ends, the clearance time would be reduced to half of 116.7 days. In that case, both backhoe loaders would meet between Node 9 and Node 10. However, equal division of the segment is often impractical in hilly terrain due to topographical constraints, limited availability of debris dumping sites, and instances where sections of the road are completely damaged or washed away by landslides, necessitating hillside excavation and the construction of temporary access roads. In addition, variations in population density along different road segments, as well as the severity of damage, significantly influence the allocation of resources.

Further, as alternative routes are often unavailable in such hilly terrains, effective planning and optimal resource allocation become essential. After an earthquake, moving resources such as backhoe loaders can be difficult or even impossible, because most roads in these areas are single- or two-lane with very limited space on either side. The narrow width of these roads also makes it operationally challenging to deploy more than one backhoe loader at the same location due to limited maneuvering space. Road blockages must therefore be cleared first to allow resources to reach critical locations, which can significantly delay deployment. In the hypothetical example discussed, the communities located near Node 9 are the last to regain access to basic healthcare facilities, even though they are geographically closer to IIT Mandi, when debris is cleared only from Node 1 and Node 10. This emphasizes the need for pre-earthquake planning and optimized allocation of backhoe loaders and other clearance equipment in hilly terrains where alternative routes are scarce. Strategic deployment of such resources prior to an earthquake event can significantly reduce recovery times, enhance road network functionality, and ensure equitable access to critical services for all communities.

5. Summary and conclusion

This study proposes methodologies for identifying critical road segments in the Indian Himalayan Region (IHR) and estimating their expected functional recovery times for different hazard scenarios. The methodologies enable rapid quantitative identification of vulnerable nodes, supporting pre-hazard planning and prioritization of recovery efforts. Debris clearance rate, a key factor in recovery planning, was estimated for earthquake-induced building debris and earthquake-

induced landslide debris, where the earthquake was considered as the primary hazard, and the landslide as the secondary hazard. The application of the debris clearance rate, obtained during field survey from practicing professionals, is demonstrated through a hypothetical case study, which highlights the importance of deploying additional resources in parallel to accelerate debris clearance operations and reduce the functional recovery time of the critical road segments. By integrating these insights into emergency planning, stakeholders can more effectively identify critical paths, allocate resources, and expedite the restoration of road services.

Further studies could explore the relationship between the blockage factor and building damage states based on post-hazard observations and/or numerical analyses. Moreover, future research could build on this work by incorporating real-time monitoring through satellite imagery, ground sensors, etc., to keep road blockage data updated. The approach can also be expanded to account for blockages caused by other predominant hazards in hilly regions, such as flash floods, rockfalls, and snow avalanches, thereby increasing its applicability. In addition, the debris removal problem could be formulated as an optimization task by incorporating factors such as available equipment, workforce, and budget, which would make the framework more generalizable and adaptable to real-world constraints. Testing the methodology in different regions and collecting post-disaster field data would help refine the framework and further strengthen its value as a practical decision-making tool for resilience planning in hilly and hazard-prone regions.

CRediT authorship contribution statement

Rahul Kumar: Writing – original draft, Visualization, Methodology, Investigation, Formal analysis, Data curation, Conceptualization. **Mahipal Kulariya:** Writing – original draft, Visualization, Methodology, Investigation, Formal analysis, Data curation, Conceptualization. **Sandip Kumar Saha:** Writing – review & editing, Visualization, Supervision, Project administration, Methodology, Funding acquisition, Conceptualization.

Data availability statement

Some or all data, models, or code that support the findings of this study are available from the corresponding author upon reasonable request.

Funding

The authors acknowledge the support of the Science and Engineering Research Board (SERB), now part of the Anusandhan National Research Foundation (ANRF), Government of India, to conduct the rapid visual screening for vulnerability assessment of the buildings reported in this study, through a core research grant with sanction number CRG/2023/006660.

Declaration of competing interest

The authors declare that they have no known competing financial interests or personal relationships that could have appeared to influence the work reported in this paper.

References

Aggarwal, Y., Baddipalli, S., Saha, S.K., 2024. Construction practices and seismic vulnerability of buildings in the Indian Himalayan Region: a case study. Nat. Hazards Rev. 25 (2), 05024002. https://doi.org/10.1061/NHREFO.NHENG-1902.

Alizadeh, D., Dodge, S., 2025. Disaster vulnerability in road networks: a data-driven approach through analyzing network topology and movement activity. Int. J. Geogr. Inf. Sci. 39 (5), 1035–1056. https://doi.org/10.1080/13658816.2024.2411001.

Argyroudis, S.A., Pitilakis, K., 2011. In: Seismic risk performance of urban transportation systems considering site effects and interaction with the built environment. Tokyo Institute of Technology, Tokyo, Japan. https://www.researchgate.net/publication/271840855_SEISMIC_RISK_PERFORMANCE_OF_URBAN_TRANSPORTATION_SYSTEMS_CONSIDERING_SITE_EFFECTS_AND_INTERACTION_WITH_THE_BUILT_ENVIRONMENT.

Argyroudis, S.A., 2010. Seismic Vulnerability and Risk of Transportation Networks in Urban Environment. PHD Thesis,. School of Civil Engineering, Aristotle University of Thessaloniki, Greece.

Aydin, N.Y., Duzgun, H.S., Heinimann, H.R., Wenzel, F., Gnyawali, K.R., 2018. Framework for improving the resilience and recovery of transportation networks under geohazard risks. Int. J. Disaster Risk Reduct. 31, 832–843. https://doi.org/10.1016/j.ijdrr.2018.07.022.

BIS, 2016. IS 1893 Part 1: Criteria for Earthquake Resistant Design of Structures. Bureau of Indian Standards, New Delhi, India. https://law.resource.org/pub/in/bis/S03/is.1893.1.2002.pdf.

Çelik, M., Ergun, O., Keskinocak, P., 2015. The post-disaster debris clearance problem under incomplete information. Oper. Res. 63 (1), 65–85. https://doi.org/10.1287/opre.2014.1342.

Chen, M., Mangalathu, S., Jeon, J.S., 2023. Betweenness centrality-based seismic risk management for bridge transportation networks. Eng. Struct. 289, 116301. https://doi.org/10.1016/j.engstruct.2023.116301.

Das, R., 2020. Approach for measuring transportation network resiliency: a case study on Dhaka, Bangladesh. Case Stud. Transp. Pol. 8 (2), 586–592. https://doi.org/10.1016/j.cstp.2020.04.001.

Devi, M., Gupta, V., Solanki, A., Sarkar, K., 2022. Assessment of slope instability using kinematic analysis and finite element modelling in the main central thrust zone, Bhagirathi valley, NW Himalaya. Himal. Geol. 43 (1), 51–60. https://www.researchgate.net/publication/391532854_Assessment_of_slope_instability_using_Kinematic_analysis_and_Finite_Element_Modelling_in_the_Main_Central_Thrust_zone_Bhagirathi_Valley_NW_Himalaya.

Dong, B.X., Shan, M., Hwang, B.G., 2022. Simulation of transportation infrastructures resilience: a comprehensive review. Environ. Sci. Pollut. Control Ser. 29 (9), 12965–12983. https://doi.org/10.1007/s11356-021-18033-w.

Esfahani, Z.K., Akbarzadeh, M., Corman, F., 2024. On the importance of adopting a multi-centrality approach to detecting the vital nodes of urban road networks. Sustain. Anal. Model. 4, 100031. https://doi.org/10.1016/j.samod.2024.100031.

Fang, C., Chu, Y., Fu, H., Fang, Y., 2022. On the resilience assessment of complementary transportation networks under natural hazards. Transport. Res. Transport Environ. 109, 103331. https://doi.org/10.1016/j.trd.2022.103331.

Fang, Y.P., Pedroni, N., Zio, E., 2016. Resilience-based component importance measures for critical infrastructure network systems. IEEE Trans. Reliab. 65 (2), 502–512. https://doi.org/10.1109/TR.2016.2521761.

FEMA P154, 2003. Rapid Visual Screening of Buildings for Potential Seismic. Hazards: a Handbook. Disaster Prev. Manag. 12 (4). https://doi.org/10.1108/dpm.2003.07312dab.014.

Freckleton, D., Heaslip, K., Louisell, W., Collura, J., 2012. Evaluation of resiliency of transportation networks after disasters. Transp. Res. Rec. 2284, 109–116. https://doi.org/10.3141/2284-13.

Froude, M.J., Petley, D.N., 2018. Global fatal landslide occurrence from 2004 to 2016. Nat. Hazards Earth Syst. Sci. 18 (8), 2161–2181. https://doi.org/10.5194/nhess-18-2161-2018.

Furno, A., Faouzi, N.E.E., Sharma, R., Zimeo, E., 2021. Graph-based ahead monitoring of vulnerabilities in large dynamic transportation networks. PLoS One 16 (3), e0248764. https://doi.org/10.1371/journal.pone.0248764.

Gokalp, C., Patil, P.N., Boyles, S.D., 2021. Post-disaster recovery sequencing strategy for road networks. Transp. Res. Part B Methodol. 153, 228–245. https://doi.org/10.1016/j.trb.2021.09.007.

Google Earth (GE), 2025. Retrieved from *Google Earth*. https://earth.google.com/. (Accessed 12 July 2025).

HPSDMA, 2024. Himachal Pradesh state disaster management authority, profile of State. https://www.hpsdmaplan.nic.in/dams/aboutus.aspx.

HPTCP, 2022. Himachal Pradesh Town and Country Planning Rules 2014: Amended Upto 2022. Town and Country Planning Department, Shimla, Himachal Pradesh, India. https://tcp.hp.gov.in/Application//uploadDocuments/rule/Rule20221126_160623.pdf. (Accessed 12 December 2024).

Huang, Z., Loo, B.P., 2023. Vulnerability assessment of urban rail transit in face of disruptions: a framework and some lessons from Hong Kong. Sustain. Cities Soc. 98, 104858. https://doi.org/10.1016/j.scs.2023.104858.

Jana, D., Malama, S., Narasimhan, S., Taciroglu, E., 2023. Edge-based graph neural network for ranking critical road segments in a network. PLoS One 18 (12), e0296045. https://doi.org/10.1371/journal.pone.0296045.

Jin, W., Cui, P., Zhang, G., Wang, J., Zhang, Y., Zhang, P., 2023. Evaluating the post-earthquake landslides sediment supply capacity for debris flows. Catena 220 (A), 106649. https://doi.org/10.1016/j.catena.2022.106649.

Kazmi, S.Q.A., Naqvi, S.A.A., Hussain, E., Ahmed, S., 2023. Resilience assessment framework for an urban road network subjected to disruptions. KSCE J. Civ. Eng. 27 (12), 5350–5361. https://doi.org/10.1007/s12205-023-1669-5.

Kim, J., Deshmukh, A., Hastak, M., 2018. A framework for assessing the resilience of a disaster debris management system. Int. J. Disaster Risk Reduct. 28, 674–687. https://doi.org/10.1016/j.ijdrr.2018.01.028.

Kulariya, M., Kumari, M., Saha, S.K., 2026. A critical appraisal of local construction practices in the Western Himalayan Region with a focus on the performance of buildings under multiple hazards. J. Struct. Des. Construct. Pract. 31 (1), 05025011. https://doi.org/10.1061/JSDCCC.SCENG-1759.

Kulariya, M., Saha, S.K., 2024a. Efficient intensity measures for vulnerability assessment of reinforced concrete buildings under flow-type and slow to moderately moving landslides. Structures 69, 107267. https://doi.org/10.1016/j.istruc.2024.107267.

Kulariya, M., Saha, S.K., 2024b. Failure mechanism and landslide fragility of reinforced concrete buildings considering uncertain flow properties. Georisk 18 (4), 779–805. https://doi.org/10.1080/17499518.2024.2337377.

Kulariya, M., Aggarwal, Y., Kashyap, H., Saha, S.K., 2024a. Rapid visual screening methodology for multi-hazard vulnerability assessment of reinforced concrete buildings in hilly region. Bull. Earthq. Eng. 1–44. https://doi.org/10.1007/s10518-024-02056-y.

Kulariya, M., Thakur, V., Kumar, A., Saha, S.K., 2024b. Effect of uncertainty in geotechnical and flow parameters on landslide-induced force for building response analysis under flow-type landslides using uncoupled approach. Indian Geotech. J. 1–23. https://doi.org/10.1007/s40098-024-01074-6.

Kumar, S.A., Rajaram, C., Mishra, S., Kumar, R.P., Karnath, A., 2017. Rapid visual screening of different housing typologies in Himachal Pradesh, India. Nat. Hazards 85, 1851–1875. https://doi.org/10.1007/s11069-016-2668-3.

Lavelle, F.M., Goodhue, C., Lyons, D., 2020. Critical Path Method Assessment of Community Recovery (NIST GCR 20-023). https://doi.org/10.6028/NIST.GCR.20-023.

Liu, T., Liu, F., 2025. Graph neural networks for evaluating the reliability and resilience of infrastructure systems: a systematic review of models, applications and future directions. IEEE Access. https://doi.org/10.1109/ACCESS.2025.3611333.

Lorca, Á., Çelik, M., Ergun, Ö., Keskinocak, P., 2015. A decision-support tool for post-disaster debris operations. Procedia Eng 107, 154–167. https://doi.org/10.1016/j.proeng.2015.06.069.

Lu, Q.L., Sun, W., Dai, J., Schmöcker, J.D., Antoniou, C., 2024. Traffic resilience quantification based on macroscopic fundamental diagrams and analysis using topological attributes. Reliab. Eng. Syst. Saf. 247, 110095. https://doi.org/10.1016/j.ress.2024.110095.

Ma, G., Rezania, M., Nezhad, M.M., Hu, X., 2022. Uncertainty quantification of landslide runout motion considering soil interdependent anisotropy and fabric orientation. Landslides 19, 1231–1247. https://doi.org/10.1007/s10346-021-01795-2.

Malama, S., Jana, D., Narasimhan, S., Taciroglu, E., 2025. Risk-optimal and equitable retrofitting strategy using a Siamese graph neural network for earthquake-induced landslide hazards. J. Comput. Civ. Eng. 39 (2), 04024063. https://doi.org/10.1061/JCCEE5.CPENG-6100.

Martín, B., Ortega, E., Cuevas-Wizner, R., Ledda, A., De Montis, A., 2021. Assessing road network resilience: an accessibility comparative analysis. Transport. Res. Transport Environ. 95, 102851. https://doi.org/10.1016/j.trd.2021.102851.

Mashrur, N., Kameshwar, S., 2025. Ranking paths in road networks for equitable improvement in connectivity during disasters. Transport. Res. Transport Environ. 104611. https://doi.org/10.1016/j.trd.2025.104611.

Matisziw, T.C., Murray, A.T., 2009. Modeling s–t path availability to support disaster vulnerability assessment of network infrastructure. Comput. Oper. Res. 36 (1), 16–26. https://doi.org/10.1016/j.cor.2007.09.004.

Misra, S., Goswami, R., Mondal, T., Jana, R., 2017. Social networks in the context of community response to disaster: study of a cyclone-affected community in coastal West Bengal, India. Int. J. Disaster Risk Reduct. 22, 281–296. https://doi.org/10.1016/j.ijdrr.2017.02.017.

NDMA, 2020. A Primer on Rapid Visual Screening Consolidating Earthquake Safety Assessment Efforts in India. National Disaster Management Authority, New Delhi, India. https://ndma.gov.in/sites/default/files/PDF/Technical%20Documents/RVS-Doc-11-2020.pdf.

Nipa, T.J., Kermanshachi, S., 2022. Resilience measurement in highway and roadway infrastructures: experts' perspectives. Progr. Disast. Sci. 14, 100230. https://doi.org/10.1016/j.pdisas.2022.100230.

Pack, R.T., Tarboton, D.G., Goodwin, C.N., 1998. In: The SINMAP approach to terrain stability mapping, 2. Vancouver, British Columbia, Canada, pp. 1157–1166. https://digitalcommons.usu.edu/cee_facpub/2583/.

Peng, C., Xiang, L.Z., Zou, Q., 2013. Risk assessment of highways affected by debris flows in Wenchuan earthquake area. J. Mt. Sci. 10 (2), 173–189. https://dx.doi.org/10.1007/s11629-013-2575-y.

Raj, D., Singh, Y., Kaynia, A.M., 2024. Seismic fragility analysis of coupled building-slope systems. Earthq. Eng. Struct. Dynam. 53 (1), 116–137. https://doi.org/10.5194/nhess-25-949-2025.

Robson, E.B., Dahal, B.K., Toll, D.G., 2025. A participatory approach to determine the use of road cut slope design guidelines in Nepal to lessen landslides. Nat. Hazards Earth Syst. Sci. 25 (3), 949–973. https://doi.org/10.5194/nhess-25-949-2025.

Robson, E., Agosti, A., Utili, S., Milledge, D., 2022. A methodology for road cutting design guidelines based on field observations. Eng. Geol. 307, 106771. https://doi.org/10.1016/j.enggeo.2022.106771.

Sayarshad, H.R., Du, X., Gao, H.O., 2020. Dynamic post-disaster debris clearance problem with re-positioning of clearance equipment items under partially observable information. Transp. Res. Part B Methodol. 138, 352–372. https://doi.org/10.1016/j.trb.2020.05.011.

Serdar, M.Z., Koç, M., Al-Ghamdi, S.G., 2022. Urban transportation networks resilience: indicators, disturbances, and assessment methods. Sustain. Cities Soc. 76, 103452. https://doi.org/10.1016/j.scs.2021.103452.

Shafiei, K., Zadeh, S.G., Hagh, M.T., 2025. Robustness and resilience of energy systems to extreme events: a review of assessment methods and strategies. Energy Strategy Rev 58, 101660. https://doi.org/10.1016/j.esr.2025.101660.

Surana, M., Singh, Y., Lang, D.H., 2018. Seismic characterization and vulnerability of building stock in hilly regions. Nat. Hazards Rev. 19 (1), 04017024. https://doi.org/10.1061/(ASCE)NH.1527-6996.0000275.

Tabata, T., Onishi, A., Saeki, T., Tsai, P., 2019. Earthquake disaster waste management reviews: prediction, treatment, recycling, and prevention. Int. J. Disaster Risk Reduct. 36, 101119. https://doi.org/10.1016/j.ijdrr.2019.101119.

Tian, M., Shen, Y., Fan, L., Sheng, X.T., 2024. Copula-based probabilistic hazard assessment model for debris flow considering the uncertainties of multiple influencing factors. Adv. Civ. Eng. 6554818. https://doi.org/10.1155/2024/6554818.

Wan, Z., Mahajan, Y., Kang, B.W., Moore, T.J., Cho, J.H., 2021. A survey on centrality metrics and their network resilience analysis. IEEE Access 9, 104773–104819. https://doi.org/10.1109/ACCESS.2021.3094196.

Wang, Z., Pei, Y., Liu, J., Liu, H., 2023. Vulnerability analysis of urban road networks based on traffic situation. Int. J. Critic. Infrastruct. Protect. 41, 100590. https://doi.org/10.1016/j.ijcip.2023.100590.

Xu, X., Chen, A., Xu, G., Yang, C., Lam, W.H.K., 2021. Enhancing network resilience by adding redundancy to road networks. Transport. Res. E Logist. Transport. Rev. 154, 102448. https://doi.org/10.1016/j.tre.2021.102448.

Zhang, J., Wang, H., Huang, J., Wang, Y., Liu, G., 2023. A study on dynamic simulation and improvement strategies of flood resilience for urban road system. J. Environ. Manag. 344, 118770. https://doi.org/10.1016/j.jenvman.2023.118770.

Zhang, X., Miller-Hooks, E., 2015. Scheduling short-term recovery activities to maximize transportation network resilience. J. Comput. Civ. Eng. 29 (6), 04014087. https://doi.org/10.1061/(ASCE)CP.1943-5487.0000417.

Zou, Q., Cui, P., Zhou, G.G., Li, S., Tang, J., Li, S., 2018. A new approach to assessing vulnerability of mountain highways subject to debris flows in China. Prog. Phys. Geogr. Earth Environ. 42 (3), 305–329. https://doi.org/10.1177/0309133318770985.